Alexandria Engineering Journal 91 (2024) 457–471

Contents lists available at ScienceDirect

Alexandria Engineering Journal

journal homepage: www.elsevier.com/locate/aej

Original article

Unknown PD distinction in HVAC/HVDC by antenna-sensor with pulse sequence analysis

S. M. Kayser Azam [a], Mohamadariff Othman [a,*], Hazlee Azil Illias [a], Tarik Abdul Latef [a], Daniar Fahmi [b], Wong Jee Keen Raymond [a], Wan Nor Liza Wan Mahadi [a], A. K. M. Zakir Hossain [c], M.Z.A. Abd. Aziz [c], Ahmad Ababneh [d]

[a] Department of Electrical Engineering, Universiti Malaya, Kuala Lumpur 50603, Malaysia
[b] Department of Electrical Engineering, Sepuluh November Institute of Technology (ITS), Surabaya 60111, Indonesia
[c] Centre for Telecommunication Research & Innovation, Fakulti Teknologi Kejuruteraan Elektrik & Elektronik, Universiti Teknikal Malaysia Melaka, Jalan Hang Tuah Jaya, Durian Tunggal, Melaka 76100, Malaysia
[d] Department of Electrical Engineering, Jordan University of Science and Technology, Irbid 22110, Jordan

ARTICLE INFO

Keywords:
Partial discharge
Antenna
UHF sensor
PD detection
PD distinction
PD classification
HVAC/HVDC

ABSTRACT

Ultra-high frequency (UHF) antenna-sensors are becoming popular for non-invasive detection of unwanted electric discharge i.e., partial discharge (PD) in high-voltage (HV) systems. Early PD signals are weak for detection and classification by UHF antenna-sensors. Early PD detection and distinction are crucial to prevent equipment failure. Typically, PD signals are distinguished in HVAC by phase resolved PD (PRPD) patterns. Whereas in HVDC, some unconventional methods are applied. However, a blind distinction of PDs under unknown HVAC/HVDC conditions still remains a challenge. In this article, we address this issue by using a lotus-shaped UHF antenna-sensor for early PD detection. Unlike cut-and-try technique-based conventionally designed bio-inspired antennas, our sensor is designed by a precisely derived equivalent circuit model to systematically optimize antenna gain over size to detect early PDs. The fabricated sensor has a size of 18×11 cm^2, an average realized gain of 3.05 dBi in 740–1600 MHz frequencies, and a sensitivity index of 154.04 dBi/m^2. The sensor prototype is applied to wirelessly distinguish PD signals from unknown sources under HVAC and HVDC by pulse sequence analysis. Early detection, characterization, and distinction of unknown PD signals are ensured by the proposed sensor and interpretation technique. This work offers a distinctive PD sensing method for HVAC/HVDC converter stations.

1. Introduction

Radiometric sensors are redrawing more attention recently because they can transmit a big number of data quickly, continuously, and wirelessly which is required for smart and intelligent systems. In high-voltage (HV) systems, partial discharge (PD) is a silent threat to the HV equipment which should be continuously diagnosed at the early stage. Conventionally, the invasive electrical method by the IEC-60270 standard is used for PD diagnostics. However, such an invasive method makes HV equipment discontinuous during PD diagnostics. So, non-invasive radiometric method by the latest IEC TS 62478:2016 standard is becoming more popular in modern HV systems for its online and continuous PD diagnostic (PDD) features [1,2]. Radiometric sensors are of several types e.g., RF detector, transmission line sensor, looped wire sensor, microstrip resonator, bandpass filter, ultra-high frequency (UHF) antenna-sensor etc. Compared to other types, UHF antenna-sensors have the ability to improve received signal strength to a significantly useful level due to their radiation-gain characteristics. Meanwhile, EM sensors needs to be small for their handheld and built-in operations at indoor and outdoor HV sites. In this regard, UHF planar antennas are suitable due to low-profile characteristics [2–8].

In UHF planar antenna-sensors, the major challenge is to improve the antenna gain with respect to the antenna size reduction in a systematic way. Theoretically, PD signals can be wirelessly captured by UHF antennas that have sufficiently high gain characteristics. However, practically, when PD occurs in HV insulation defects, it radiates EM waves with very low magnitudes i.e., voltages on millivolt (mV) level, especially at the early stages of PD occurrences. These early PD signals are

---

* Corresponding author.
E-mail address: mohamadariff@um.edu.my (M. Othman).

https://doi.org/10.1016/j.aej.2024.02.013

further weakened while they propagate wirelessly through the environment until received by UHF antennas. So, early PD detection becomes extremely difficult unless the strength of received PD signals is intensified. This is conventionally done by using amplifiers after the UHF antenna. However, amplifiers are typically very expensive components which makes them not so feasible to be used in early PD detection for a large number of HV equipment. Hence, it is more convenient to design the UHF antennas with gain improvement because this enables the antenna to detect PD signals at their earliest stages. It is important to remember that early PD detection is significant for protecting HV equipment from operation failures and asset damage. Note that PD is a random event which can occur at any frequency within the UHF range. Even within the UHF range, investigation shows that most of the PDs occur between 500–1500 MHz frequencies [2]. This demands the UHF antennas for wideband characteristics to detect early PDs occurring at any frequencies. So, the gain improvement at a particular frequency or very narrow frequency-band does not justify the ability of an antenna to detect for any type of PD. It is very possible that a UHF antenna has high gain at a particular frequency but the PD it should detect is occurring at another frequency where the antenna has very low gain. In this case, the PD signal cannot be detected despite the antenna having a high gain but at a different frequency. So, to ensure any PD can be detected, a UHF antenna should cover wide bandwidth by providing a sufficiently high average realized gain throughout its bandwidth. This is why average realized gain is so important in UHF antennas for PD detection applications. According to previous investigations, generally, an antenna with an average realized gain of more than 2 dBi can suitably detect early PD signals [1,2,9,10]. However, average realized gain improvement in a wideband UHF antenna is a major challenge because gain and bandwidth have opposite relationship. Whereas UHF antennas should not occupy big areas for PD detection because there are space limitations in practical HV equipment. In fact, most of the HV equipment manufacturers provide chambers for UHF sensors that are not more than $20\times20\times20$ cm^3 in volume [2,11]. Although such space limitations are mostly for internal UHF sensors, sensor compactness is still required for external UHF sensors for their hand-help operations. Consequently, sensor compactness is also a concern in UHF antenna design for PD detection. However, antenna gain decreases with antenna size reduction unless the antenna is designed with a gain compensating mechanism. Whereas PD mostly occurs between the 0.3–1.5 GHz frequency range which further limits the compactness of UHF antennas [12]. Thus, different types of UHF antennas are proposed for PD detection by making a trade-off between gain improvement and size reduction.

For PD detection, many UHF antenna-sensors with wideband characteristics are proposed so far including Archimedean spiral antenna (ASA) [13–18], bow-tie antenna [19–21], Vivaldi antenna [22,23] etc. In terms of gain, ASA is useful for early PD detection, but it occupies a large volume in the three-dimensions. Unlike bow-tie antennas that have wide bandwidth but poor gain, Vivaldi antennas can provide sufficiently high gain with low-profile design. Note that PD can occur in any direction whereas antennas with unidirectional radiation patterns cannot detect PD from all isotropic directions. Since both ASA and Vivaldi antennas exhibit unidirectional radiation patterns, they are not the best suit for PD detection at large-scale HV sites. A planar monopole antenna (PMA) can minimize this issue [24,25] due to its omnidirectional radiation pattern. Nevertheless, gain improvement without increasing the aperture area is still a challenge in designing PMAs for PD detection applications. Gain-enhancing techniques are mostly involved with radiating patch and partial ground plane (PGP) of a PMA. For example, radiating patches of different biological shapes are useful to design PMAs for PD applications [26–28]. However, their designs are mostly geometry-based trial-and-error methods that do not offer theoretically systematic insights to improve the PMA gain. So, metamaterial sheets are added to PMAs for gain improvement [29,30]. This puts complexity both in design and system integration. Thus, for early PD detection, a systematic design procedure of PMA is highly needed so that the antenna mechanism and its gain improvement can be technically realized with clearcut theoretical basis.

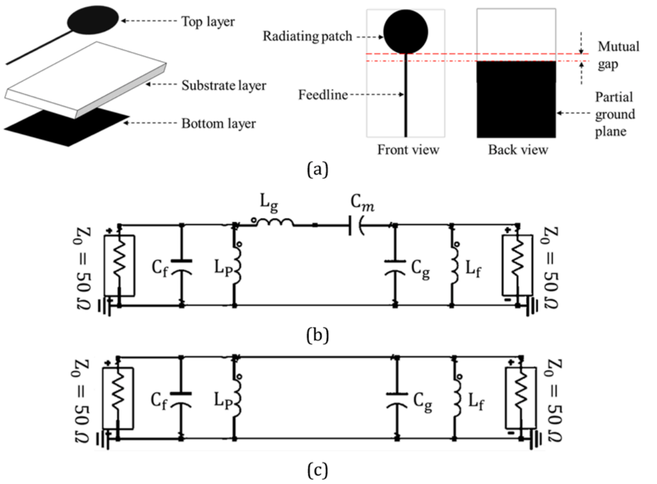

Fig. 1. Planar monopole antenna (PMA) design; (a) typical design model (b) equivalent circuit (c) resonance circuit.

In radiometric PD diagnosis, detected signals are post-processed for PD categorization. Usually, PD is categorized for HVAC by observing phase-resolved partial discharge (PRPD) patterns. Whereas PRPD is not applicable for HVDC due to the absence of signal phase in the applied DC. A few unconventional methods e.g., observing the time-resolved partial discharge (TRPD), pulse sequence analysis (PSA) etc. are used for PD categorization in HVDC. In fact, PD categorization is performed for HVAC and HVDC in two separate ways [31,32] which leads to a new challenge of distinguishing unknown PD signals at the large-scale HV stations. Such a distinctive and wireless categorization of unknown PD signals is highly applicable to HVAC/HVDC converter stations where both AC and DC equipment demand for a combined online monitoring system [33,34] which has not been researched so far in detail.

In this work, we have radiometrically distinguished unknown PD signals in different HVAC and HVDC conditions by a lotus-shaped antenna (LSA) as a UHF sensor. Unlike trial and error-based conventional bio-inspired PMAs, we have developed a systematic design procedure of the LSA so that the technique is useful for other PMAs to improve gain without increasing antenna areas. In terms of gain over area, our sensor has achieved a sensitivity of 154.04 dBi/m^2. With the antenna, unknown PDs are distinguished in different HV conditions by applying the pulse sequence analysis (PSA) as the classifier. Section II describes the design process and synthesis of the UHF sensor, section III discusses PD interpretation technique, section IV includes measurement setup, section V analyzes experimental results, and section VI concludes the article.

2. UHF antenna-sensor synthesis

The design concept of our proposed UHF antenna-sensor is inspired by the Lotus flower (*Nelumbo nucifera*) in the nature. Inspiration from natural shapes is an effective way to design a planar monopole antenna (PMA) since stepwise constructions of natural shapes make the antenna optimization convenient. However, instead of directly imitating any natural shapes as conventional bio-inspired antennas by cut-and-try approaches [26,28], we have designed our proposed UHF sensor i.e., the planar monopole antenna (PMA) by theoretically following a systematic procedure to improve antenna bandwidth and gain without increasing the antenna size. In other words, although the design shape is conventional, the proposed design technique is uniquely new and theoretically more systematic compared to other bio-inspired antenna design techniques.

We developed a lossless equivalent circuit model of a typically

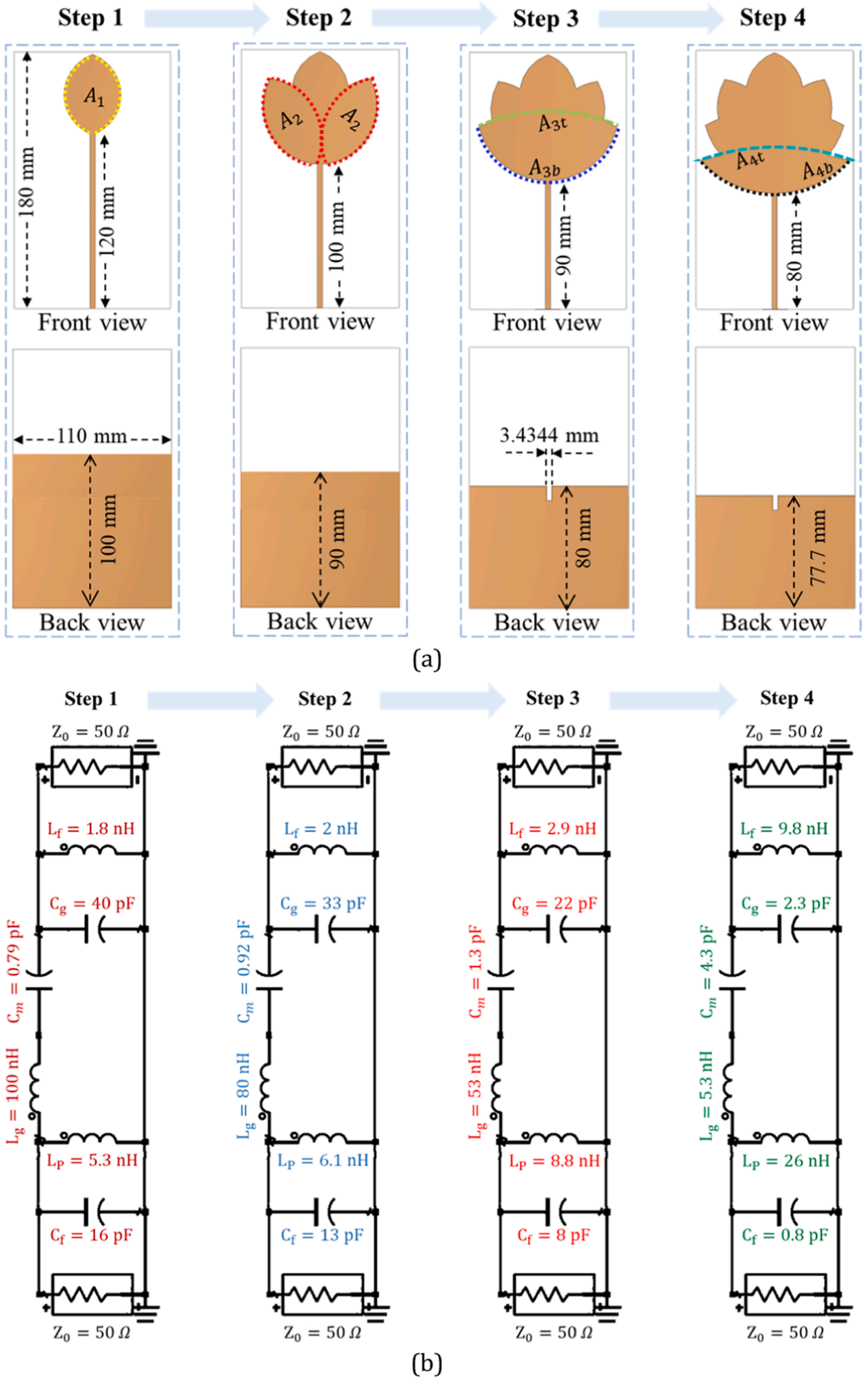

Fig. 2. Design steps (a) LSA; (b) impacts on equivalent circuit.

designed circular-patch PMA as illustrated in Fig. 1. In a typical PMA design as Fig. 1(a), three layers are stacked together, such as- a thin-conductive top layer that includes feedline and radiating patch, a dielectric substrate layer in the middle, and a thin-conductive bottom layer that includes a partial ground plane (PGP). So, different types of distributed inductances and capacitances are formed which can be represented by the lossless equivalent circuit model in Fig. 1(b). This model works as a bandpass filter circuit since bandwidth of a frequency-dependent antenna e.g., a typical PMA technically operates with band-pass characteristics. In Fig. 1(b), C_f is the effective feedline capacitance, L_P is the effective patch inductance, L_g denotes the effective PGP inductance, C_m indicates the capacitance formed by the mutual gap between the radiating patch on top layer and the PGP on the bottom layer, C_g symbolizes the effective PGP capacitance, and L_f denotes the effective feedline inductance.

We Hence, using the circuit model of Fig. 1(b), the fundamental frequency (f_0) of the PMA can be found as [10],

$$f_0 = \frac{1}{2\pi\sqrt{L_T \times C_T}}. \tag{1}$$

Here, L_T is the total inductance and C_T is the total capacitance. If we calculate L_T and C_T from Fig. 1(b), then L_g and C_m are cancelled out which turns the f_0 into is the frequency of resonance (f_R) as,

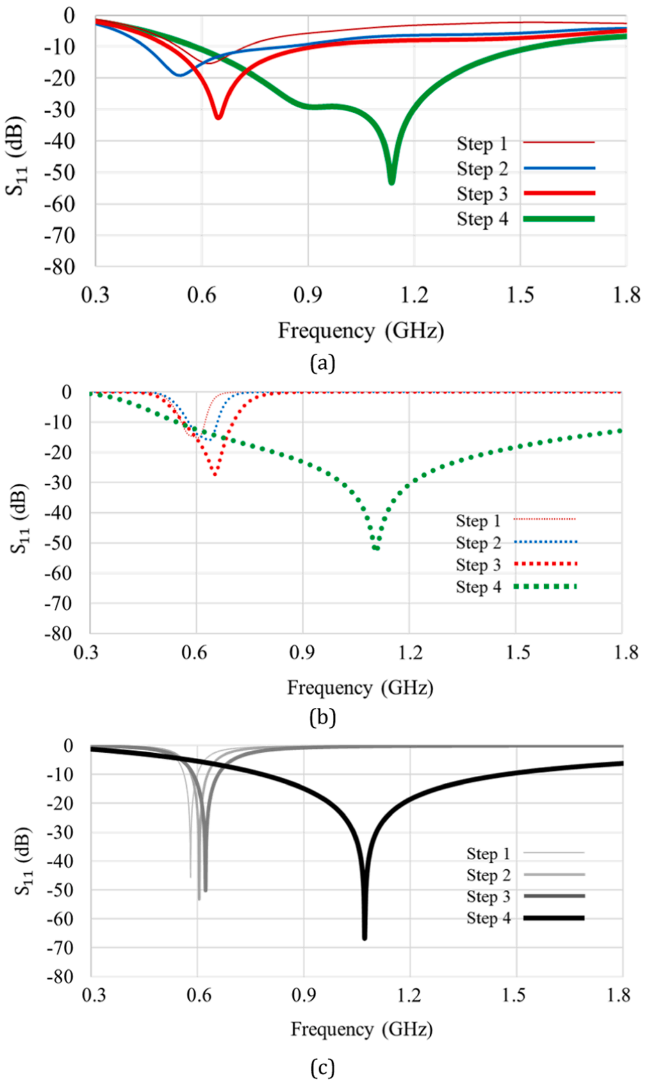

(a)

(b)

(c)

Fig. 3. Simulated S11 (a) LSA; (b) equivalent circuit; (c) resonance circuit.

$$f_R = \frac{1}{2\pi\sqrt{[C_f + C_g] \times \left[\frac{L_p \times L_f}{L_p + L_f}\right]}}. \tag{2}$$

In this expression, it is clear that L_g and C_m have no direct impact on controlling the resonant frequency of PMA. Thus, the model turns into a resonance circuit as in Fig. 1(c). Still, L_g and C_m must have impacts on bandwidth and gain of PMA which are optimized in our proposed design by using Fig. 1(b) and (c).

Now, we designed our PMA as a Lotus-shaped antenna (LSA) which took four successive stages for its optimization. Fig. 2 demonstrates the LSA design steps and their impacts on corresponding equivalent circuits. Our design steps resemble blossom stages of a Lotus flower as illustrated in Fig. 2(a). On step 1, a basic PMA, just like the PMA in Fig. 1(a), was designed by a Lotus bud-shaped radiating patch. The feedline is of microstrip type which has a width of w_f. This width is found from the formula below [12],

$$w_f = \frac{7.48 \times h}{e^{\left(Z_0 \frac{\sqrt{\varepsilon_r + 1.41}}{87}\right)}} - 1.25 \times t. \tag{3}$$

Here, Z_0 is the characteristics impedance of the feedline which is matched with the standard normalization impedance of 50 Ω to reduce in-band return loss, h is the substrate height, ε_r is the relative dielectric constant of the substrate, and t is the trace thickness of each conductive layer. In our design, we utilized a substrate with $h = 1.52$ mm, $\varepsilon_r = 3.5$, $t = 0.035$ mm, and a tangent loss of 0.0027. So, from (3), the width of feedline is determined as 3.4344 mm.

For precisely built-in electromagnetic design and simulation tools that are close to the prototype performance, CST Studio Suite 2021 and Advanced Design System 2021 were utilized to design and simulate the LSA. Length and width of the LSA are 180 mm and 110 mm, respectively. For all steps, we extracted their corresponding equivalent circuits by following Fig. 1(b) which are presented in Fig. 2(b). We observed the S_{11} parameter response of a designed layout first, and then calculated its corresponding inductances and capacitances by utilizing (1) and the conventional formula of bandpass filters [35]. On step 1, the Lotus bud-shaped radiating patch is designed by an arc A_1 that has a radius of 30 mm. In this case, the PGP is 100 mm long which results in a high L_g. On the other hand, a weak C_m is formed by the 20 mm mutual gap between the steeply designed patch on the top plane and the PGP. Fig. 3 shows the stepwise S_{11} responses of LSA layout, equivalent circuit, and resonance circuit to demonstrate the impacts of L_g and C_m. On step 2, two Lotus petal-shaped elements are designed by an arc A_2 that has a radius of 40 mm. Meanwhile, PGP length decreased to 90 mm. As a result, L_g is decreased and C_m is slightly increased. Whereas there are decreases of C_g and C_f, and increases of L_P and L_f during step 2. On step 3, another element is designed by two arcs i.e., top arc $A_{3\,t}$ that has a radius of 50 mm and bottom arc A_{3b} that has a radius of 100 mm. As seen in Fig. 2(b), all the inductances and capacitances including L_g and C_m are impacted in the similar way of step 2. However, the bandwidth is still not wide on step 3. So, we truncated a slot on the PGP below the feedline direction which has a length of 10 mm and an equal width of the feedline. This was done so that the overall impedance is intensively perturbed by any small changes made in the next step for obtaining the desired bandwidth.

Thus, on step 4, we added one more element that is designed by two arcs i.e., top arc $A_{4\,t}$ that has a radius of 70 mm and bottom arc A_{4b} that has a radius of 200 mm. Notice, the A_{4b} has a longer radius because such a gradually bent arc brings an exponential effect on the overall inductances and capacitances. This effect on step 4 can be understood by observing the subsequent S_{11} responses in Fig. 3(a) and (b). It is important to notice that S_{11} responses of the LSA layout design and equivalent circuit agree with each other during all steps. On the other hand, Fig. 3(b) and (c) correspond to each other in terms of resonance but their bandwidths are different. Bandwidths in Fig. 3(b) are wider than in Fig. 3(c). So, by observing Fig. 3, Fig. 2, and Fig. 1, it is evident that L_g and C_m have a strong impact on improving the bandwidth despite they have no direct impact on the frequency of resonance as implied in (2). Now, the LSA is simulated to observe realized gain, radiation patterns, and surface current distribution which are shown in Fig. 4. On step 4, the maximum realized gain is obtained as 3.96 dBi while the average realized gain is found as 2.30 dBi. It is obvious from Fig. 4(a) that the overall realized gain has reached the highest value on step 4. This indicates another direct impact of L_g and C_m on the LSA. As shown in Fig. 4 (b), the feedline injects the maximum current into the body of the radiating patch. This allows the antenna to operate in the radiation mode instead of the guided field mode.

Simulated radiation patterns indicate that the LSA has an omnidirectional radiation pattern which is useful for PD diagnosis regardless of angular position of the PD occurrence. Unlike geometric shape-dependent conventional PMA designs where mostly trial-and-error techniques are followed, we have designed our proposed UHF sensor by following a systematic procedure based on the equivalent circuit method. Furthermore, this method can be utilized for designing PMAs that have different geometric shapes than bio-inspired designs [10]. In our method, theoretical insights are precisely derived on each step of the design which give clear indications of how to improve bandwidth and gain even without increasing the size of the antenna. This method is suitable especially for PD detection applications where antenna size is

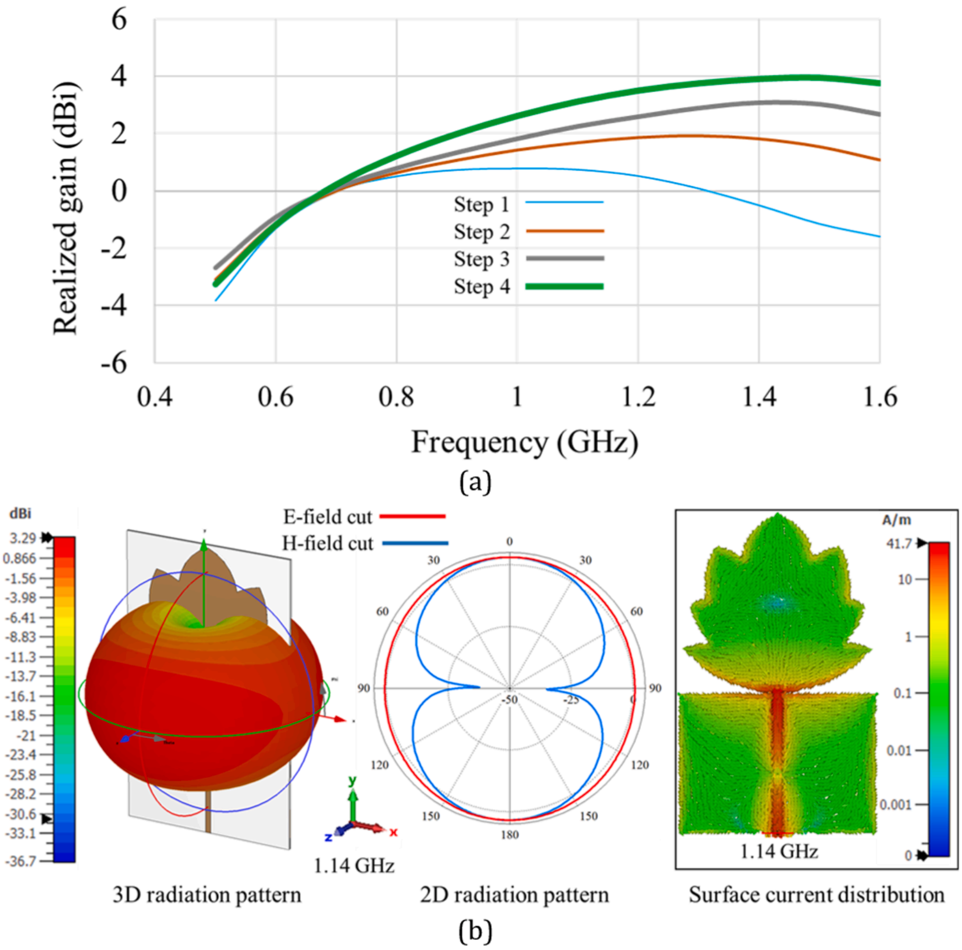

Fig. 4. Design for wide impedance bandwidth; (a) stages (b) simulated S_{11}.

limited but gain and bandwidth need to be optimized.

Conventionally, effective height of a UHF antenna is used to express its sensitivity for PD detection [2]. However, effective height measurement requires a complex arrangement of the Gigahertz Transverse Electromagnetic (GTEM) cell which is expensive and commercially unpopular. Whereas measuring gain is quite common in antenna applications. So, for PD detection applications, we utilized a new index of antenna sensitivity (S_A) by considering average realized gain (G_{RA}) and physical aperture area (A_P) as [3],

$$S_A = \left(\frac{G_{RA}}{A_P}\right). \tag{4}$$

In this work, A_P is defined as the surface area of the antenna which is obtained by multiplying the length and width of a planar antenna or calculating the circular area from the radius of a spiral antenna. Notice that S_A requires no additional measurement or arrangement such as a GTEM cell other than a typical antenna measurement setup. S_A is technically quite analogous to the effective height since they both consider incident signals over the physical area of an antenna. It is to remember that S_A should be calculated for antennas that have the same range of operating frequencies. So, this new index of S_A is technically justifiable to evaluate UHF antennas for PD sensing applications since the frequency range of PD occurrence remains the same. However, antennas with different bandwidth should be evaluated by another index that comprises other parameters of antenna i.e., total efficiency ($\eta_{Avg.}$), fractional bandwidth (FBW), and wavelength (λ_0) to maintain consistency and avoid any bias. According to [3], we can evaluate our sensor by calculating the antenna-sensor's Figure of Merit (FoM_S) that includes the above stated parameters as,

$$FoM_S = 10 \times \log_{10}\left[\left(\frac{\eta_{Avg.} \times FBW}{100\% \times 100\%}\right) \Big/ \left(\frac{4\pi \times A_P}{{\lambda_0}^2}\right)\right]. \tag{5}$$

In (5), $\eta_{Avg.}$ is an important parameter but it is often not revealed by conventional UHF sensors possibly due to their low $\eta_{Avg.}$. Note that a UHF sensor may have high gain but still failing to detect early PD since its total efficiency is poor.

3. Partial discharge interpretation technique

PD signals are detected by the LSA and then collected by the oscilloscope. Then, the collected data are post-processed for PD interpretation. We-PSA technique-based algorithm, as reported in [36], is adopted to interpret the PD signals. A short elaboration of the PSA technique is illustrated in Fig. 5.

The PSA algorithm calculates magnitude and occurrence time of consecutive PD signals. In other words, this algorithm counts the peak and time of a signal and compares these two parameters with the same parameters of the following signals. This computation is applied for a large number of data as illustrated in Fig. 5(b). First, the data number is determined to read the total amount of data. Then, the amplitude peak and occurrence time are obtained. Next, the interpretation quantities are processed and stored until the same steps are applied to the total amount of data. Finally, the interpretation quantities are combined to plot the expected results. Conventionally, this algorithm is applied to interpret PD in HVDC only. Whereas in HVAC, PRPD patterns are generated by a different algorithm. In both cases, PD signals from UHF method are compared with PD signals from the IEC 60270 method where electric

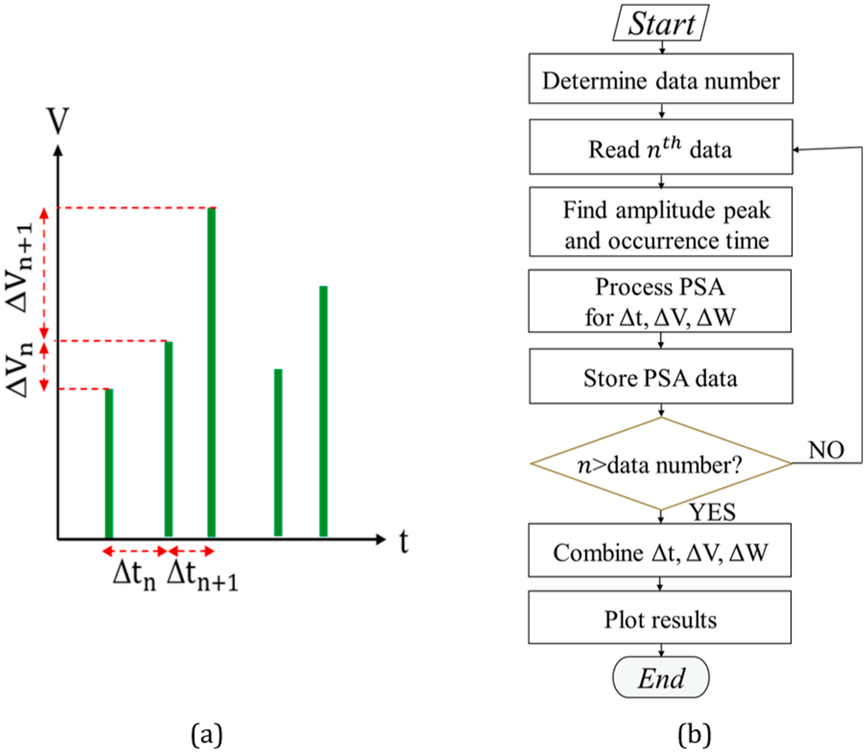

Fig. 5. PSA technique (a) concept; (b) interpretation process.

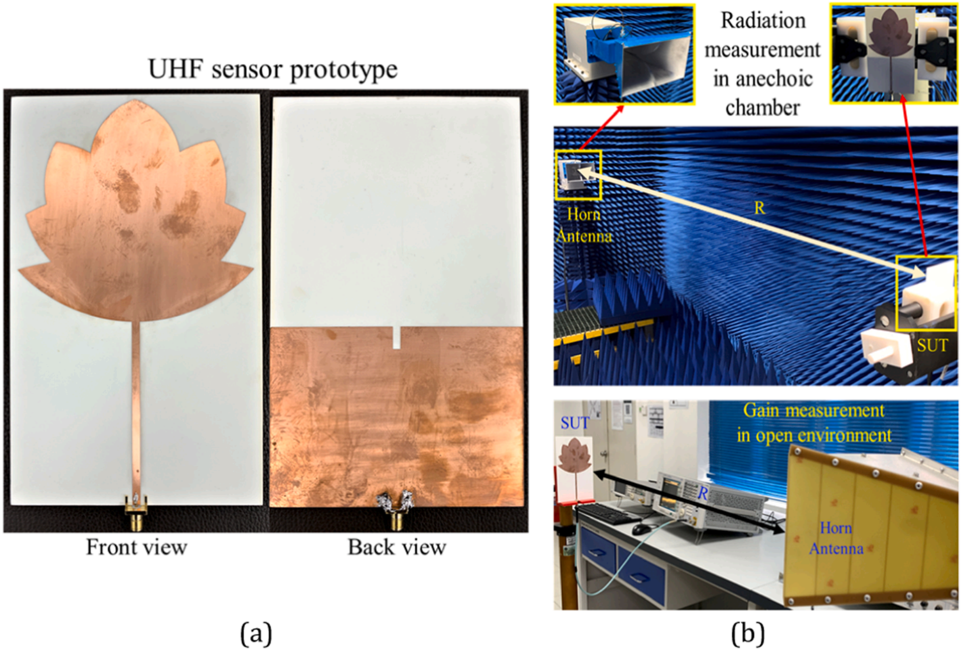

Fig. 6. Antenna-sensor (a) prototype; (b) radiation measurement.

charges from PD events are directly and invasively collected to determine signal amplitudes. So, for charge-based calibration, PD interpretation by UHF method becomes dependent on IEC 60270 method since UHF method does not offer any charge value-based calibration process as the IEC 60270 method does. The UHF method typically relies on the voltage amplitude of PD signals collected by the oscilloscope because direct collection of electric charge is not possible in EM wireless technique i.e., UHF method. Therefore, we have utilized voltage amplitude difference (ΔV) by the PSA to interpret PD both for HVAC and HVDC. So, the dependency on IEC 60270 method becomes no longer mandatory which is highly demanded by the latest IEC TS 62478:2016 standard for non-invasive PD diagnostics. Fig. 5(b) illustrates our interpretation process. We computed an extra quantity of ΔW as a product of ΔV and Δt. It is numerically understandable that the multiplication of two variables provides more distinction of changes than their separate representations. So, for a slight variation of ΔV and Δt, the ΔW gives more accurate and distinguishable patterns than extracting conventional patterns from ΔV and Δt only [36]. We applied ΔW for the distinction of

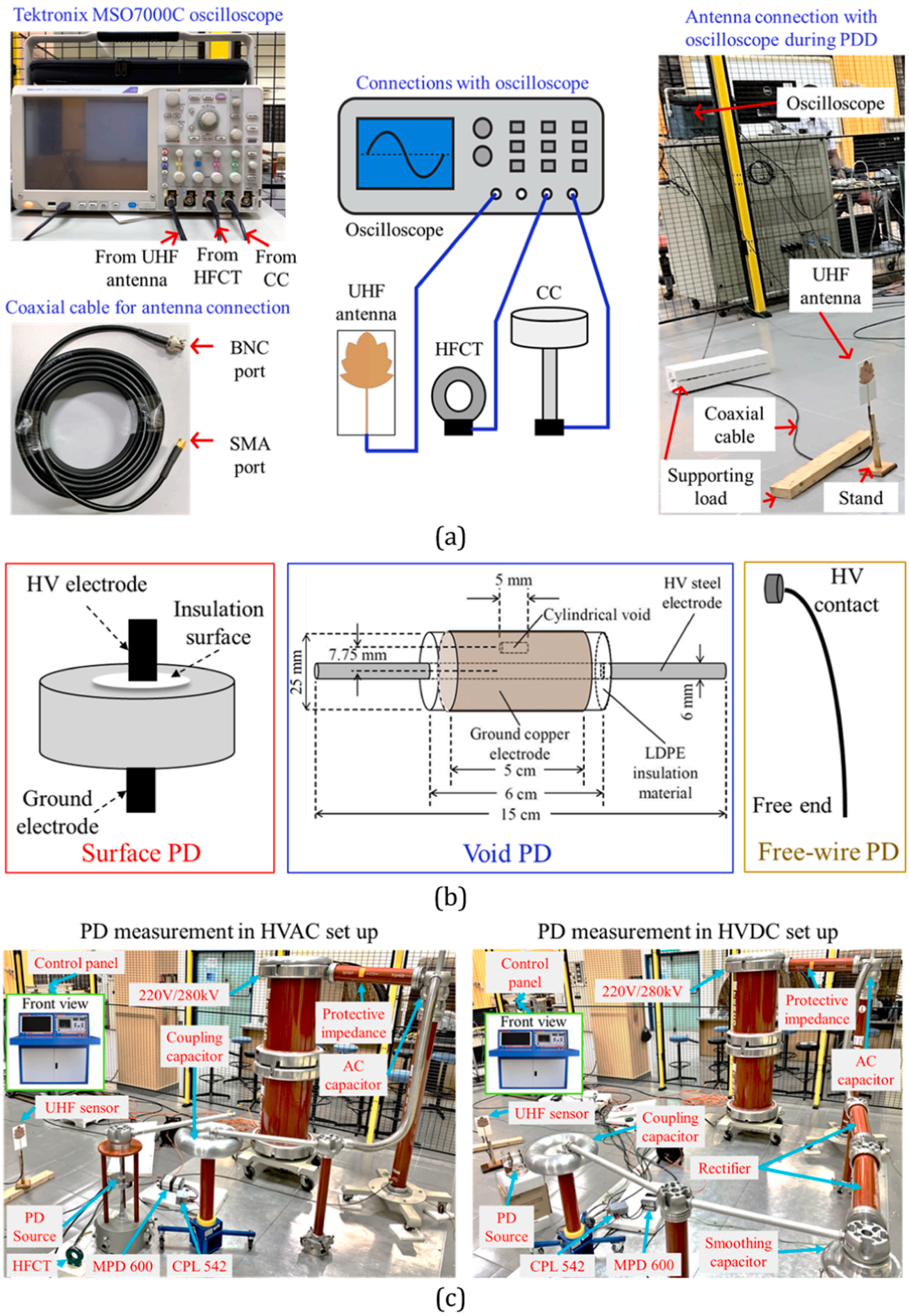

Fig. 7. PD measurement (a) UHF antenna connection with oscilloscope; (b) PD sources [38]; (c) experimental set up.

an unknown PD signal to determine whether it comes from a HVAC, HVDC+, or HVDC− source. In this case, we observe ΔW-vs-ΔV plot for PD distinction over a fixed time duration. Next, we calculated another additional quantity of ΔV_{n+1} which is plotted versus ΔV for PD categorization over a fixed time duration. Thus, with this technique, users can set a time duration to detect PD signals, and then interpret them for PD distinction and categorization.

4. Measurement setup

4.1. UHF antenna-sensor measurement setup

UHF antenna-sensor measurement was performed in the MRG Lab of the Universiti Teknikal Malaysia Melaka. Fig. 6 shows the UHF sensor prototype fabricated on a commercial Rogers RO4003C substrate and the laboratory setup for free-space radiation measurement. We measured the bandwidth by a VNA-ENA (Keysight E5071C). Then we measured gain and radiation pattern by using a signal analyzer (N9020A MXA) and horn-antennas. Note, radiation pattern was measured in an anechoic chamber, but gain was measured both inside and outside the anechoic chamber to mimic the noisy environment of HVAC/HVDC converter stations.

According to the well-known Friss formula [24], the antenna that receives EM signals from the transmitting antenna should be kept at a distance where the far-field radiation has sufficiently strength. Hence, we kept our UHF sensor at an optimum distance (R) of 4 m so that its

Table 1
V_{PP} during Minimum Detectable Charge Calibration.

Method	Surface VPP (mV) @ 50 pC	Void VPP (mV) @ 50 pC	Free-wire VPP (mV) @ 20 pC
IEC 60270	128.00	12.0	20.00
HFCT	10.60	10.20	–
LSA	11.00	10.40	12.80

far-field radiation is sufficient to receive the EM signals that are propagated from the horn antenna.

4.2. Partial discharge measurement setup

Fig. 7(a) shows the details of the connection between the LSA and the oscilloscope. It is important to note that PD signals are primarily observed as time-domain signals so that the PD events of short durations can be instantly investigated prior to data extraction. Thus, UHF antennas are connected to the oscilloscope in a way so that the PD signal received by a UHF antenna is sent to the oscilloscope for its time-domain observation. In this regard, the antenna impedance is matched with a SMA port that is terminated to one side of a low-loss coaxial cable, and another side of the coaxial cable is terminated to a BNC port that connects the oscilloscope with same impedance matching. This is how a PD signal, as an EM signal, is collected by a UHF antenna and observed in time-domain by the oscilloscope. Typically, amplifiers are used between the low-gain antenna and the oscilloscope to boost up received signal level for early PD detection. However, as extensively clarified in Section 2, the proposed antenna is designed with sufficient gain to deliver PD signal directly to the oscilloscope through the coaxial cable as shown in Fig. 7(a). A high frequency current transformer (HFCT) and a coupling capacitor (CC) are also connected to the oscilloscope. For partial discharge measurement, we performed experiments in the laboratory where a 200 V/280 kV transformer was used to generate HVAC and rectifiers were used to convert into HVDC. Since discharge probability is more in the air [8], we conducted experiments under air-insulation. Fig. 7(b) shows our PD measurement with three different PD sources such as a surface discharge, a void discharge, and a free-wire discharge both in HVAC and HVDC. Fig. 7(c) illustrates these PD sources where PD was generated from a polymer disc (5 mm diameter and 2 mm thickness), a cell of void immersed into oil (to avoid unwanted PDs), and a 0.5 m long free-wire of 2 mm diameter.

Since there is no standard calibration process for UHF method yet, we had to calibrate the test-cell first by using Omicron 542 calibrator according to the IEC 60270 calibration standard. It is done so because if the UHF antenna can detect calibrated pulses, then it can be further utilized to analyze the detected PD signals in a similar way of PD analysis by the conventional method [37]. So, with our sensor, first we

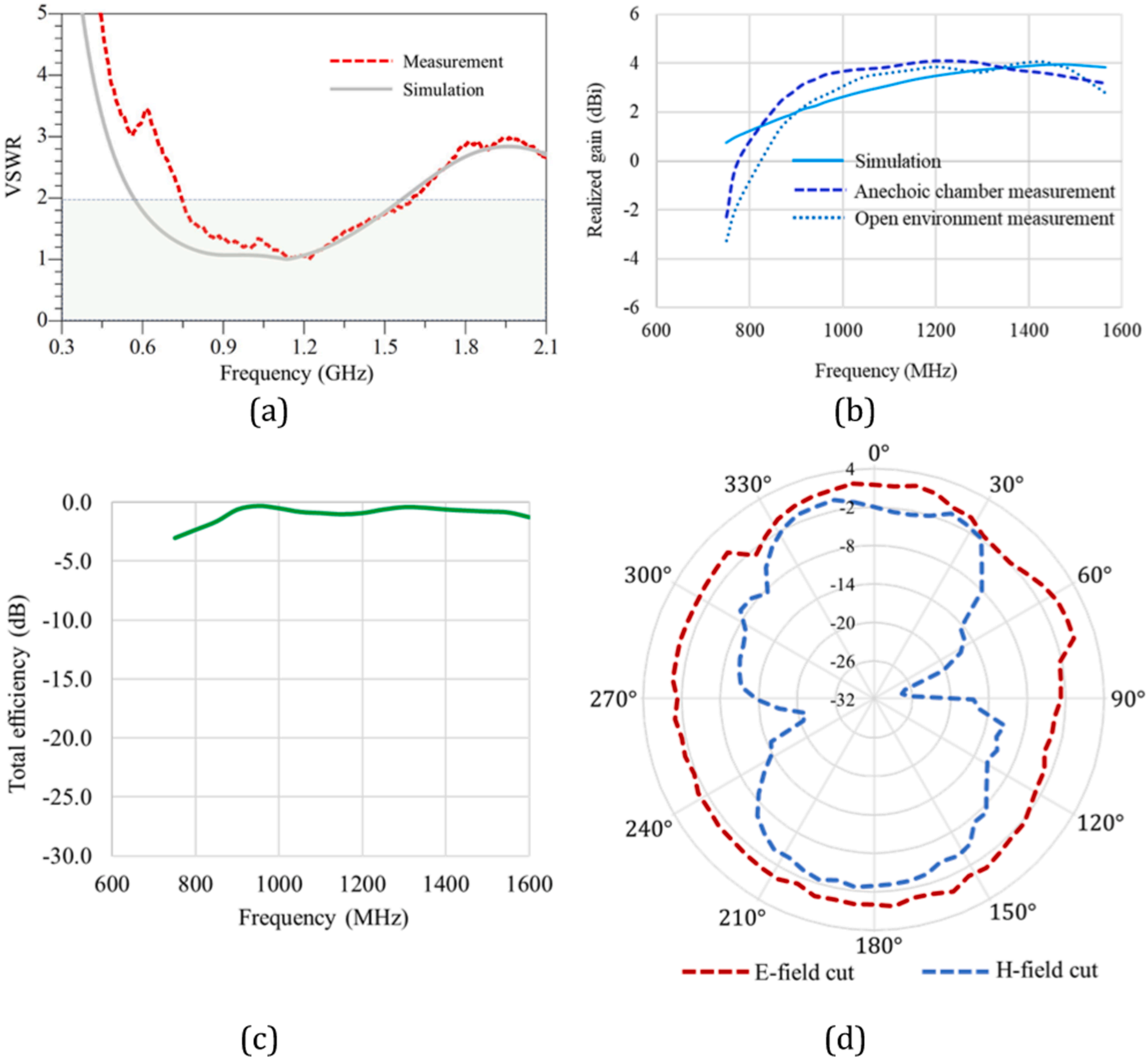

Fig. 8. Measured performance of LSA prototype (a) VSWR; (b) realized gain; (c) total efficiency; (d) radiation pattern at f_0.

Table 2
Performance Comparison of UHF Antenna-Sensors.

Ref.	Dimension	BW (GHz)	G_{RA} (dBi)	RPD	S_A (dBi/ m^2)	FoM_S (dB)
[13]	$\pi\times202\times16$ cm^3	0.60–1.70	4.00	Uni	31.83	−16.67
[14]	$\pi\times15.42\times8$ cm^3	0.50–5.00	2.04	Uni	27.38	–
[15]	$\pi\times192\times11$ cm^3	0.50–2.00	4.75	Uni	41.88	–
[17]	$\pi\times192\times11$ cm^3	0.75–2.00	4.70	Uni	41.44	−16.77
[24]	30×30 cm^2	0.31–1.48	2.00	Omni	22.22	–
[25]	24×20 cm^2	0.35–1.38	3.50	Omni	72.91	−7.18
[26]	34×14 cm^2	0.34–8.00	3.63	Omni	76.26	–
LSA	18×11 cm^2	0.74–1.60	3.05	Omni	154.04	−7.54

detected calibrated pules and compared with the IEC 60270 method and an HFCT, and then we detected actual PD signals.

Table 1 shows the peak-to-peak amplitude (V_{PP}) of a signal detected by three methods during the minimum detectable charge calibration to all three PD sources. It is found that the LSA has more accuracy than the HFCT.

To make EM shielding of the PD measuring environment, our laboratory was enclosed by a Faraday cage which protects the test-bench from unwanted signals that have frequencies lower than the UHF range. The test-bench is surrounded by a cage that is made by grounded metallic grills. This protects the laboratory from unwanted EM impulses at lower frequencies than the UHF range. Therefore, despite telecommunication signals are still available inside the cage, the test-bench becomes shielded. The UHF sensor was optimally kept at 1 m distance

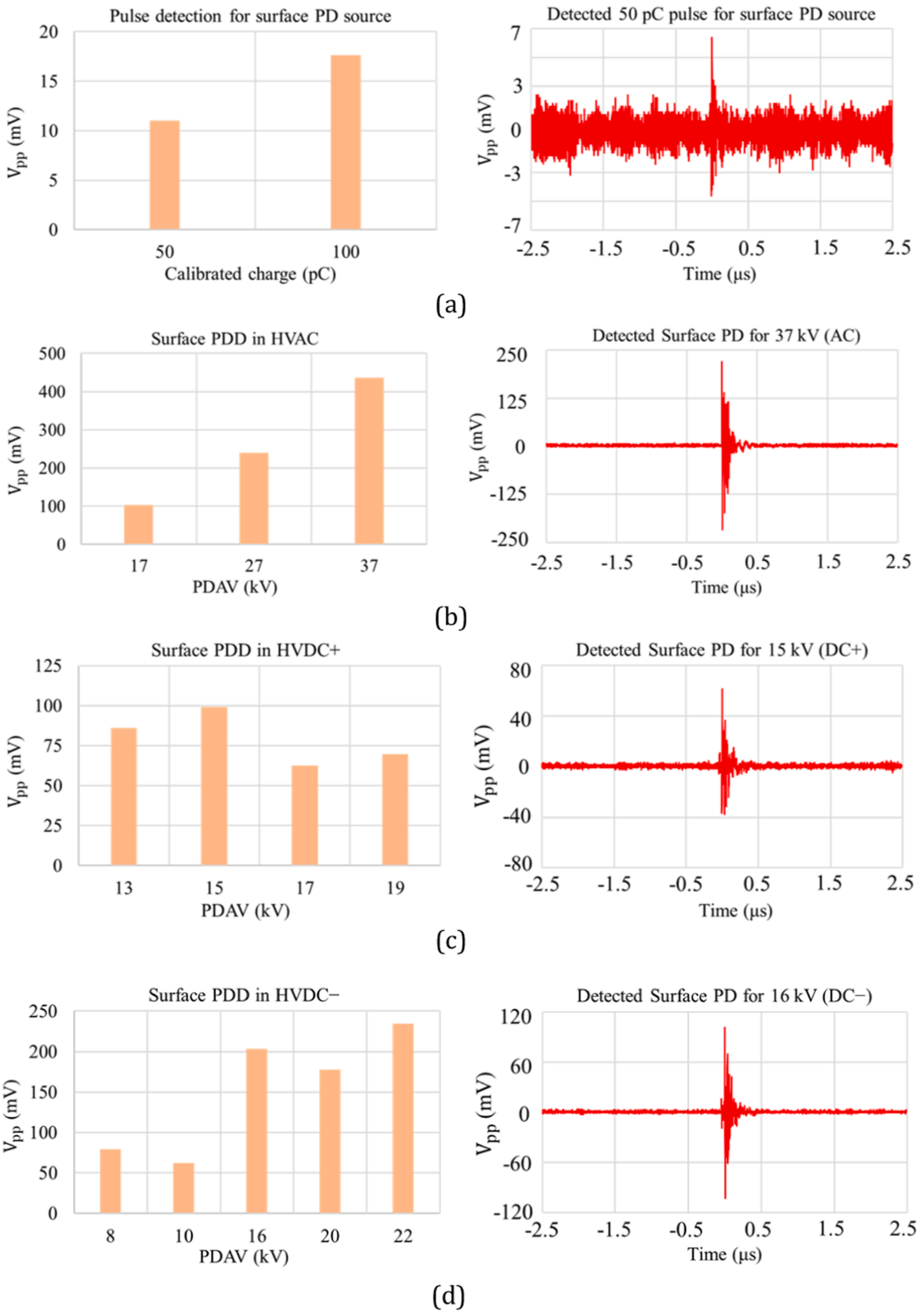

Fig. 9. Surface PDD: (a) pulses (b) HVAC (c) HVDC+ (d) HVDC−.

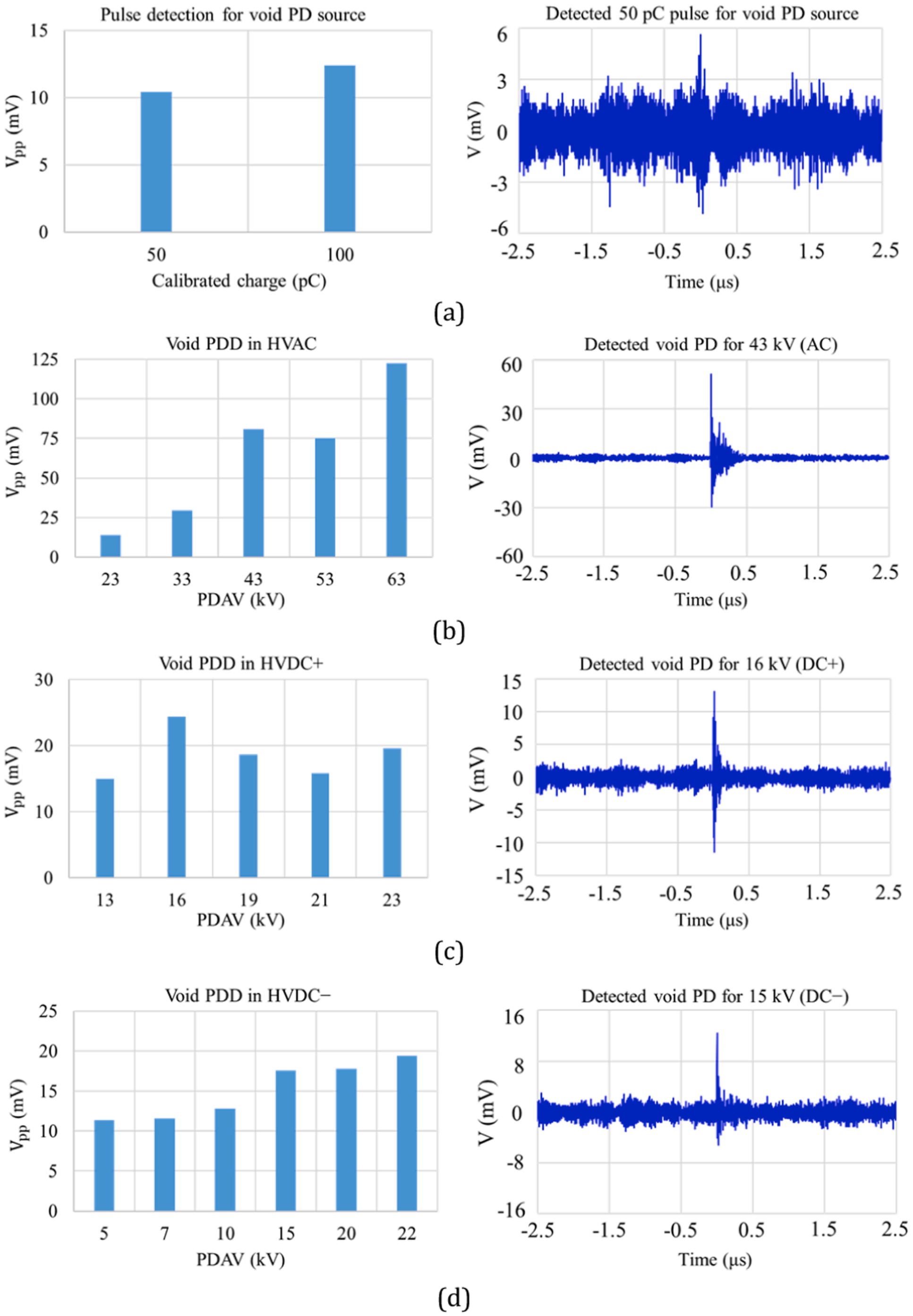

Fig. 10. Void PDD: (a) pulses (b) HVAC (c) HVDC+ (d) HVDC−.

from a PD source by considering the far-field radiation characteristics of the LSA. Since the proposed antenna-sensor is electrically small, the 1 m distance is set within its calculated far-field region by following the antenna theory [2]. PD data collected by the UHF sensor was transferred to an oscilloscope through a low-loss co-axial cable. Then, the data was analyzed in MATLAB software for comprehensive interpretations.

5. Experimental results and analyses

5.1. UHF antenna-sensor performance

The proposed UHF sensor was first tested for its impedance characteristics and then radiation performance. Gain is measured inside and outside the anechoic chamber to observe the real-world scenario. Fig. 8 shows the measured performance of the antenna-sensor. It is noteworthy that in terms of the impedance bandwidth, if a UHF sensor covers a frequency range of 0.5–1.5 GHz, then it can practically detect most of the PD signals in the UHF range. Again, a UHF sensor is suggested to have an average realized gain of 2 dBi with an omnidirectional radiation pattern so that it can detect weak signals of early PD occurrences [2]. As seen from Fig. 8(b), our sensor prototype has an average realized gain of 3.05 dBi over an operating bandwidth (VSWR<2) of 745–1600 GHz frequencies. The sensor prototype has a maximum gain of 4.07 dBi and a minimum VSWR of 1.004. Measured results have a decent agreement with simulated results even though a slight deviation is seen due to fabrication tolerance. Fig. 8(c) shows the total efficiency (86.5% on

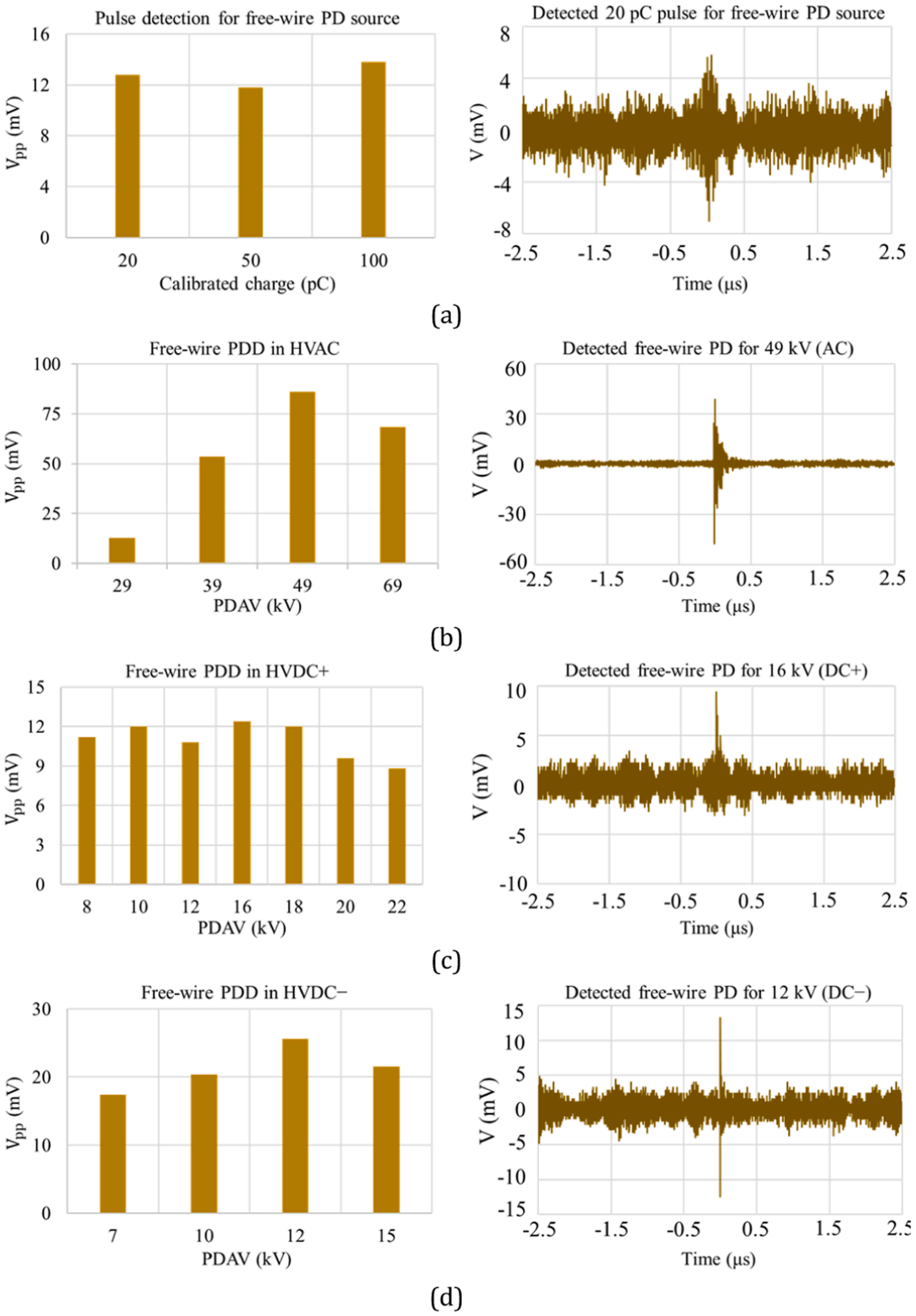

Fig. 11. Free-wire PDD: (a) pulses (b) HVAC (c) HVDC+ (d) HVDC−.

average). Fig. 8(d) shows an omnidirectional pattern as previously in Fig. 4(b).

Table 2 compares performance of the LSA prototype with some recently proposed antennas for PD detection in terms of their physical dimensions, bandwidth (BW), average realized gain (G_{RA}), radiation pattern direction (RPD) etc. According to the antenna sensitivity index derived in (4), our proposed LSA has higher S_A than others for PD detection applications. Also, the FoM_S is reasonably high which justifies the LSA's overall antenna performance regardless of any application bias.

5.2. *Characterization of partial discharge detection*

Before PD distinction and categorization, signals detected by the UHF sensor should be analyzed first for a partial discharge characterization which will help us to understand the detected signal properties in terms of the different PD sources and the variation of partial discharge applied voltage (PDAV) from HVAC, HVDC+, and HVDC− supplies. As discussed before, we calibrated PD sources with charges and observed the level of corresponding pulse detected by the UHF sensor. Regarding the PD characterization, we observed PD sources one by one. A characterization of PD detection (PDD) for the surface discharge is presented in Fig. 9 which includes the detected signals against the corresponding calibrated charges and PDAVs. Also, a time domain signal is provided

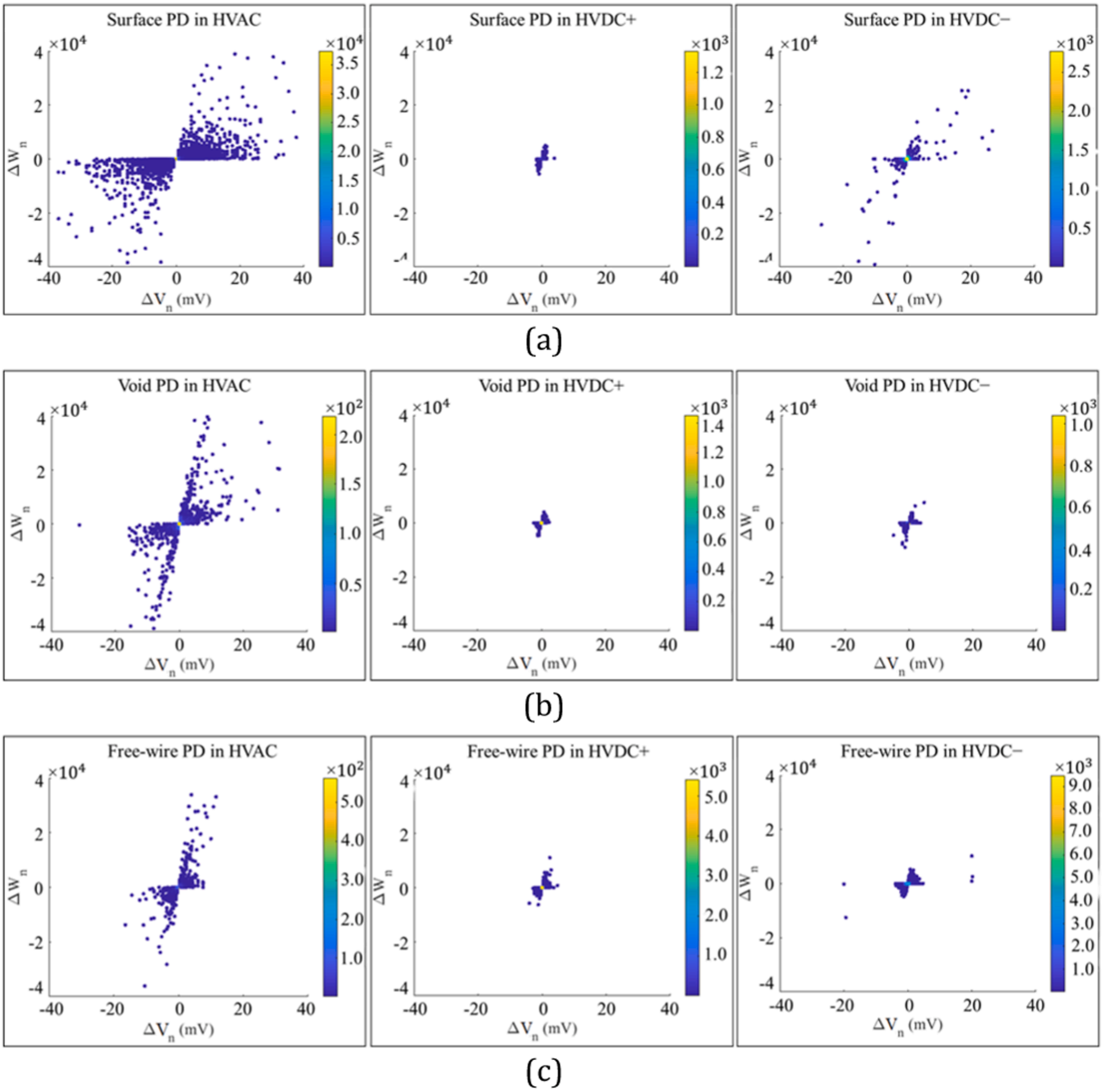

Fig. 12. PD distinction: (a) for surface (b) for void (c) for free-wire.

with each graph in the figure for a better observation.

Pulses of charge calibrations are detected by UHF antennas through the Fresnel region because electrically short antennas, such as UHF planar sensors, encounter the strongest radiating far-field and the weakest near-field in the Fresnel region [39]. UHF antennas with high sensitivity can detect such a pulse which indicates their early PD detection capability. As in Fig. 9(a) for surface discharge, the UHF sensor detected pulses of 50 pC and 100 pC calibrate charges. The minimum charge was 50 pC for which the sensor detected a signal of 11 mV whereas a signal of 17.6 mV was detected for 100 pC calibrated charge. This indicates that our proposed UHF sensor has compatibility of detecting early PDs both in HVAC and HVDC. As in Fig. 9(b), PDD of surface discharge in HVAC is characterized. The applied voltage for which an initially detectable PD occurs i.e., early PD voltage (EPDV) was found at 17 kV and the highest voltage before the breakdown was observed at 37 kV. A linear rise in the detected PD signal (V_{PP}) was found with the increase of PDAV. When HVDC+ was applied to the same discharge model, EPDV dropped down to 13 kV and no linear relationship was found between PDAV and V_{PP}. When HVDC− was applied, EPDV was decreased further to 8 kV as shown in Fig. 9(d). For surface discharge, notice that V_{PP} is found higher in HVAC than in HVDC+ and HVDC−. In HVDC−, PDAV before breakdown is higher than HVDC+.

In Fig. 10, we observe characterization of the void PDD. With a minimum calibrated pulse of 50 pC, V_{PP} is found to be 10.4 mV which is similar to the surface PDD. In HVAC, EPDV and maximum PDAV of void PDD are higher than surface PDD while V_{PP} is lower during the void PDD. One of the reasons for it is that EM radiation during a PD is absorbed more in void model than in surface discharge model since the void was immersed into insulation oil inside a glass container. This is noticed when void PDD is performed in HVDC+ and HVDC− as in Figs. 10(c) and 11(d). Note that EPDV dropped to 5 kV during the void PDD in HVDC−.

Characterization of the free-wire PDD is illustrated in Fig. 11. A pulse from the minimum calibrated charge of 20 pC was detected by our sensor with a V_{PP} of 12.8 mV. Note, minimum calibrated charge required for PDD to a free-wire is lower than surface and void defects because the free-wire is a completely exposed conductor without any contact of insulating materials. However, the free-wire acts like a monopole antenna when PD occurs after HVAV is provided to it. Hence, the PD is radiated electromagnetically in surroundings of the free-wire which in turn increases EPDV and decreases V_{PP} during PDD especially in HVAC because EM radiation is more affected by the polarity reversal of HVAC. As seen in Fig. 11(b), V_{PP} is only 12.8 mV despite the EPDV is at 29 kV. In HVDC+, V_{PP} is of low amplitude and does not vary

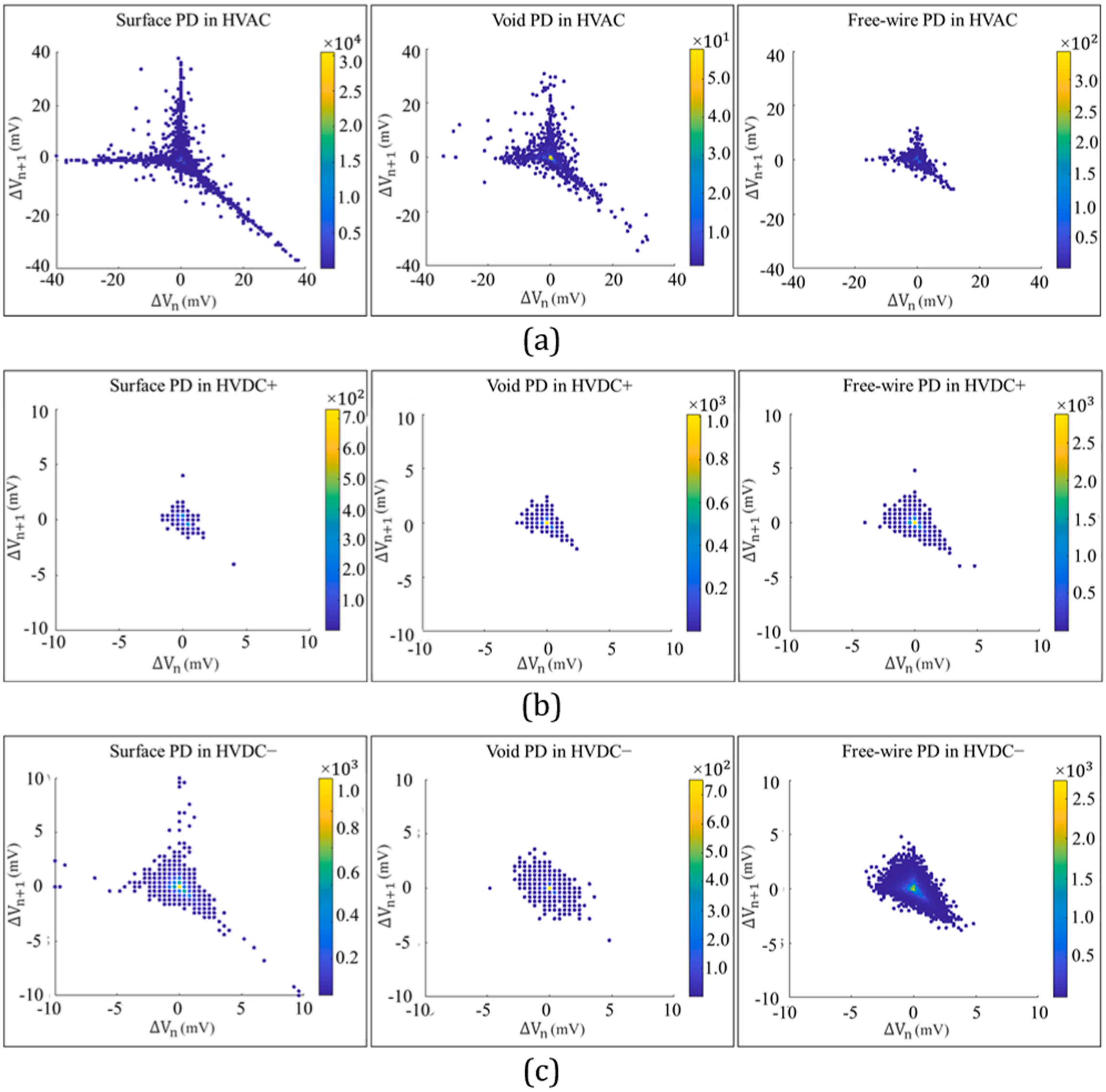

Fig. 13. PD categorization: (a) in HVAC (b) in HVDC+ (c) in HVDC−.

much with the PDAV as shown in Fig. 11(c). Whereas in HVDC−, V_{PP} mostly increases when PDAV is increased but the breakdown occurs earlier. It is obvious that we did not use the same PDAV consistently throughout the entire experiment because the EPDV does not remain the same but rather differs from one PD source to another and one HV supply type to another.

5.3. *Distinction of HV supplies in partial discharges*

Based on the PDD characterization, it is evident that PD has different signal amplitudes with different HV supplies and PD sources. In other words, for a specific time, PD signal behaves differently with two variables- HV supply type and PD source type. First, we have to apply three different HV supplies i.e., HVAC, HVDC+, and HVDC− one by one on the same PD source over a fixed time duration to obtain their corresponding patterns from our proposed PSA-based technique. So, response from the PD source can be easily recognized next time by identifying an unknown HV supply type.

We have observed patterns from three different PD sources to provide a comprehensive PD distinction for unknown HV supplies. In this regard, we have observed the ΔW-vs-ΔV plot by maintaining the same scaling for all extracted patterns from different PD responses so that these patterns are compared and recognized as in illustrated in Fig. 12. It is important to remember that ΔW is a product of the amplitude variation (ΔV) and PD occurrence time variation (Δt) of consecutive PD events, as discussed earlier in Section 3. In Fig. 12(a), ΔW-vs-ΔV patterns of surface PD in HVAC, HVDC+, and HVDC− are observed. PD occurrence pattern is found to be the widest in HVAC and narrowest in HVDC+ since amplitude variation in HVAC during surface discharge is higher. In HVDC−, the pattern is scattered along their occurrence points. This implies that PD is most occurred in HVAC and least occurs in HVDC+ while the occurrence rate is moderate in HVDC−. Such occurrence rate is also observed for the other two PD sources i.e., void and free-wire as shown in Fig. 12(b) and (c), respectively. However, in terms of the patterns, their distinction is pretty evident. For void PD, HVAC pattern is not as wide as before, rather, more scattered towards lines in upward and downward directions. Whereas HVDC+ pattern is like a tilted bow-tie and HVDC− pattern resembles a jumping dolphin. For the free-wire PD, HVAC pattern is irregularly scattered at the bottom, but the top is steeper with a narrow funnel shape. The HVDC+ pattern resembles a scorpion while the HVDC− pattern resembles a butterfly flying in between two columns of bees. Thus, since these patterns are observed for the same period of time and plot-scaling, they can be useful for recognizing unknown PDs.

Table 3
Comparison of PD Diagnosis by UHF Antenna-Sensors.

Ref.	PDD	PDC	PDC in HVDC	HV distinction
[13]	✅	✅	❌	❌
[24]	✅	❌	❌	❌
[25]	✅	✅	❌	❌
[26]	✅	✅	✅	❌
This work	✅	✅	✅	✅

5.4. Categorization of partial discharges

Once HV supply type is recognized through PD distinction, then the PD source can be reaffirmed by the PD categorization. In this regard, we have categorized PD by applying the same HV supply to three different PD sources over the same time period as mentioned earlier. As in Fig. 13, we applied HVAC first, then HVDC+, and finally HVDC− to observe different PD patterns of surface, void, and free-wire defects each time.

For each HV supply, plot-scaling is kept same to all patterns from three different PD sources so that categorization is accurately understood. This time we use ΔV_n-vs-ΔV_{n+1} plot to improve the accuracy of PD categorization. As seen in Fig. 13(a), PD occurs most frequently on surface defect than others when HVAC is applied. To better understand, we can imagine three directions along these patterns in Fig. 13. For surface PD, the pattern is more scattered along those directions than scattering in a random way which is observed for void PD. For free-wire PD, the pattern is much concentrated. It is evident from Fig. 13(a) that PD occurs most frequently for surface and least frequently for free-wire when HVAC is applied. The opposite is observed when HVDC+ supply is applied. As noticed in Fig. 13(b), PD occurs least frequently for surface defect and most frequently for free-wire defect during the HVDC+ supply. Although void pattern in this case is less than free-wire pattern and more than surface pattern, it has no minor scattering like the other two patterns have along the three directions on the plot. When HVDC− supply is applied, then these defects exhibit different patterns as observed in Fig. 13(c). In HVDC−, PD is most frequent for free-wire defect with a highly concentrated triangular-shaped pattern and least frequent for void defect with random pattern. For surface PD, the pattern slightly spreads to three directions.

By observing these patterns obtained from ΔV_n-vs-ΔV_{n+1} plot, PD categorization (PDC) is accomplished both in HVAC and HVDC by applying a single classifier. Table 3 compares our technique with others that best fit the scope of this work. It is evident from the comparison on Table 3 that this is the only work that offers detection and categorization of PD both in HVAC and HVDC and makes distinction for an unknown PD signal to recognize whether it is occurred because of the HVAC, HVDC+, or HVDC− power supply.

6. Conclusion

In this work, we introduced a UHF antenna-sensor by a new design method which works within 740–1600 MHz frequencies. We experimentally validated the sensor protype by measuring partial discharges for three different defects i.e., surface, void, and free-wire in HVAC, HVDC+, and HVDC− supplies. Key contributions of this work are summarized in following points:

•equivalent circuit model-based new design method is introduced for planar monopole antennas,

•antenna-sensor's gain over size, i.e., sensitivity index is increased to 154.04 dBi/m^2 for limited space PD sensing application while the figure of merit is enhanced to −7.54 dB for the antenna-sensor's overall performance improvement,

•a new interpretation technique of partial discharge is introduced that does not depend on the charge amplitude of PD signals and the type of HV supply,

•partial discharge detection is characterized for three different defects in HVAC and HVDC,

•distinction patterns for those defects are extracted to recognize whether a PD is due to HVAC or HVDC,

•PD is categorized in HVAC/HVDC by one classifier.

In future, big data should be collected by the proposed technique to incorporate machine learning approaches for precise PD classifications. Also, this work can be utilized for PD localization according to the new IEC TS 62478:2016 standard. We believe this work will play a taboo-breaking role in overcoming the challenge of making a universal PD classifier both for HVAC and HVDC systems.

Declaration of Competing Interest

The authors declare that they have no known competing financial interests or personal relationships that could have appeared to influence the work reported in this paper.

Acknowledgments

This work was funded by the Universiti Malaya (UM), Malaysia through the UM International Collaboration Grant of IMG003–2023, RU Geran - Fakulti Program of GPF008A-2023, and the Malaysian Ministry of Higher Education through the Malaysian International Scholarship (MIS) 2022.

References

[1] S. Kaziz, M.H. Said, A. Imburgia, B. Maamer, D. Flandre, P. Romano, F. Tounsi, Radiometric Partial Discharge Detection: A Review, Energies 16 (2023) 1978, https://doi.org/10.3390/en16041978.

[2] S.M.K. Azam, M. Othman, H.A. Illias, T. Abdul Latef, M. Tariqul Islam, M. Fadzil Ain, Ultra-high frequency printable antennas for partial discharge diagnostics in high voltage equipment, Alexandria Eng. J. 64 (2023) 709–729, https://doi.org/10.1016/j.aej.2022.11.026.

[3] M.S. Islam, S.M.K. Azam, A.K.M. Zakir Hossain, M.I. Ibrahimy, S.M.A. Motakabber, A low-profile flexible planar monopole antenna for biomedical applications, Eng. Sci. Technol. Int. J. 35 (2022) 101112, https://doi.org/10.1016/j.jestch.2022.101112.

[4] M.M.O. Harbaji, A.H. Zahed, S.A. Habboub, M.A. AlMajidi, M.J. Assaf, A.H. El-Hag, N.N. Qaddoumi, Design of Hilbert Fractal Antenna for Partial Discharge Classification in Oil-Paper Insulated System, IEEE Sens. J. 17 (2017) 1037–1045, https://doi.org/10.1109/JSEN.2016.2638804.

[5] Z. Shu, W. Wang, C. Yang, Y. Guo, J. Ji, Y. Yang, T. Shi, Z. Zhao, Y. Zheng, External Partial Discharge Detection of Gas-Insulated Switchgears Using a Low-Noise and Enhanced-Sensitivity UHF Sensor Module, IEEE Trans. Instrum. Measur. 72 (2023) 1–10, https://doi.org/10.1109/TIM.2023.3277980.

[6] J. Choi, S. Park, J. Lee, K.-Y. Jung, UHF-Printed Monopole Filtenna for Partial Discharge Detection with LTE Signal Suppression, J. Electromagn. Eng. Sci. 23 (2023) 180–187, https://doi.org/10.26866/jees.2023.2.r.158.

[7] S. Dhara, C. Koley, S. Chakravorti, UHF Sensors Based Localization of Partial Discharge Sources in Air-Insulated Electrical Substation Using TDOA and Relative RSS Information, IEEE Trans. Instrum. Measur. 72 (2023) 1–9, https://doi.org/10.1109/TIM.2023.3253876.

[8] J. Sun, N. Wu, Y. Fan, D. Lei, S. Yang, X. Guo, H. Wang, S. Song, Partial discharge characteristics of free moving metal particles in gas insulated systems under DC and AC voltages, IET Generation, Transmission Distribution 17 (2023) 1047–1058, https://doi.org/10.1049/gtd2.12501.

[9] G.V.R. Xavier, H.S. Silva, E.G. da Costa, A.J.R. Serres, N.B. Carvalho, A.S. R. Oliveira, Detection, Classification and Location of Sources of Partial Discharges Using the Radiometric Method: Trends, Challenges and Open Issues, IEEE Access 9 (2021) 110787–110810, https://doi.org/10.1109/ACCESS.2021.3102888.

[10] S.M.K. Azam, M. Othman, H.A. Illias, T.A. Latef, W.N.L.W. Mahadi, D. Fahmi, A.K. M.Z. Hossain, M.F. Ain, Planar Sensor for Noise Cancellation During Partial Discharge Detection in Open Substation, IEEE Sens. J. 23 (2023) 15552–15562, https://doi.org/10.1109/JSEN.2023.3279861.

[11] H. Chai, B.T. Phung, S. Mitchell, Application of UHF Sensors in Power System Equipment for Partial Discharge Detection: A Review, Sensors 19 (2019) 1029, https://doi.org/10.3390/s19051029.

[12] S.M.K. Azam, M. Bin Othman, T. Abdul Latef, H.A. Illias, M. Fadzil Ain, Y. Qasaymeh, Wideband Antenna with UHF Sensor Applicability for HV Equipment in Smart Grid, Proc. Int. Conf. Artificial Life Robotics 27 (2022) 162–168, https://doi.org/10.5954/ICAROB.2022.OS22-3.

[13] S. Park, K.-Y. Jung, Design of a Circularly-Polarized UHF Antenna for Partial Discharge Detection, IEEE Access 8 (2020) 81644–81650, https://doi.org/10.1109/ACCESS.2020.2991158.

[14] Y.R. Yadam, R. Sarathi, K. Arunachalam, Planar Ultrawideband Circularly Polarized Cosine Slot Archimedean Spiral Antenna for Partial Discharge Detection, IEEE Access 10 (2022) 35701–35711, https://doi.org/10.1109/ACCESS.2022.3163303.

[15] P. Wang, S. Ma, S. Akram, P. Meng, J. Castellon, Z. Li, G.C. Montanari, Design of an Effective Antenna for Partial Discharge Detection in Insulation Systems of Inverter-fed Motors, IEEE Trans. Indus. Electr. 69 (2022) 13727–13735, https://doi.org/10.1109/TIE.2021.3130335.

[16] K.C. Ghanakota, Y.R. Yadam, S. Ramanujan, V.P.V.J., K. Arunachalam, Study of Ultra High Frequency Measurement Techniques for Online Monitoring of Partial Discharges in High Voltage Systems, IEEE Sens. J. 22 (2022) 11698–11709, https://doi.org/10.1109/JSEN.2022.3172173.

[17] P. Wang, S. Ma, S. Akram, K. Zhou, Y. Chen, M.T. Nazir, Design of Archimedes Spiral Antenna to Optimize for Partial Discharge Detection of Inverter Fed Motor Insulation, IEEE Access 8 (2020) 193202–193213, https://doi.org/10.1109/ACCESS.2020.3033300.

[18] C. Zachariades, R. Shuttleworth, R. Giussani, T.-H. Loh, A Wideband Spiral UHF Coupler With Tuning Nodules for Partial Discharge Detection, IEEE Trans. Power Delivery 34 (2019) 1300–1308, https://doi.org/10.1109/TPWRD.2018.2883828.

[19] T. Rhamdhani, U. Khayam, A. Zaeni, Improving Antenna Performance by Combining Dipole and Bowtie Antenna for Partial Discharge Measurement in Gas Insulated Switchgear, IEEE Int. Conf. Power Eng. Appl. (ICPEA) 2022 (2022) 1–4, https://doi.org/10.1109/ICPEA53519.2022.9744679.

[20] J.P. Uwiringiyimana, U. Khayam, Measurement of Partial Discharge in Air Insulation by using UHF Double Layer Bowtie Antenna with Modified Wings Edges, Int. Conf. Electr. Eng. Inform. (ICEEI) 2019 (2019) 228–233, https://doi.org/10.1109/ICEEI47359.2019.8988866.

[21] C. Zachariades, R. Shuttleworth, R. Giussani, A Dual-Slot Barrier Sensor for Partial Discharge Detection in Gas-Insulated Equipment, IEEE Sens. J. 20 (2020) 860–867, https://doi.org/10.1109/JSEN.2019.2943625.

[22] J. Zhang, X. Zhang, S. Xiao, Antipodal Vivaldi Antenna to Detect UHF Signals That Leaked Out of the Joint of a Transformer, Int. J. Antennas Propag. 2017 (2017) e9627649, https://doi.org/10.1155/2017/9627649.

[23] R. Albarracin, G. Robles, J.M. Martinez-Tarifa, J. Ardila-Rey, Separation of sources in radiofrequency measurements of partial discharges using time–power ratio maps, ISA Trans. 58 (2015) 389–397, https://doi.org/10.1016/j.isatra.2015.04.006.

[24] G.V.R. Xavier, E.G. da Costa, A.J.R. Serres, L.A.M.M. Nobrega, A.C. Oliveira, H.F. S. Sousa, Design and Application of a Circular Printed Monopole Antenna in Partial Discharge Detection, IEEE Sens. J. 19 (2019) 3718–3725, https://doi.org/10.1109/JSEN.2019.2896580.

[25] Y. ZHANG, P. LAZARIDIS, R. ABD-ALHAMEED, I. GLOVER, A compact wideband printed antenna for free-space radiometricdetection of partial discharge, Turk. J. Electr. Eng. Comput. Sci. 25 (2017) 1291–1299, https://doi.org/10.3906/elk-1510-100.

[26] J. do, N. Cruz, A.J.R. Serres, A.C. de Oliveira, G.V.R. Xavier, C.C.R. de Albuquerque, E.G. da Costa, R.C.S. Freire, Bio-inspired Printed Monopole Antenna Applied to Partial Discharge Detection, Sensors 19 (2019) 628, https://doi.org/10.3390/s19030628.

[27] L.A.M.M. Nobrega, G.V.R. Xavier, M.V.D. Aquino, A.J.R. Serres, C.C. R. Albuquerque, E.G. Costa, Design and Development of a Bio-Inspired UHF Sensor for Partial Discharge Detection in Power Transformers, Sensors 19 (2019) 653, https://doi.org/10.3390/s19030653.

[28] G.V.R. Xavier, A.C. de Oliveira, A.D.C. Silva, L.A.M.M. Nobrega, E.G. da Costa, A.J. R. Serres, Application of Time Difference of Arrival Methods in the Localization of Partial Discharge Sources Detected Using Bio-Inspired UHF Sensors, IEEE Sens. J. 21 (2021) 1947–1956, https://doi.org/10.1109/JSEN.2020.3019760.

[29] G.V.R. Xavier, A.J.R. Serres, E.G. da Costa, A.C. de Oliveira, L.A.M.M. Nobrega, V. C. de Souza, Design and Application of a Metamaterial Superstrate on a Bio-Inspired Antenna for Partial Discharge Detection through Dielectric Windows, Sensors 19 (2019) 4255, https://doi.org/10.3390/s19194255.

[30] R.V. de Andrade Lira, A.L.P. de Siqueira Campos, A.G. Neto, I. de Souza Silva, A.J. R. Serres, L.A.M.M. Nobrega, A.D. da Costa Silva, I.F. Carvalho, Elliptical UHF sensor for partial discharge detection, Sens. Actuat. A: Phys. 348 (2022) 113981, https://doi.org/10.1016/j.sna.2022.113981.

[31] C. Li, T. Shahsavarian, M.A. Baferani, K. Davis, Y. Cao, D. Zhang, Understanding DC Partial Discharge: Recent Progress, Challenges, and Outlooks, CSEE J. Power Energy Syst. 8 (2022) 894–909, https://doi.org/10.17775/CSEEJPES.2021.04740.

[32] R. Piccin, A.R. Mor, P. Morshuis, A. Girodet, J. Smit, Partial discharge analysis of gas insulated systems at high voltage AC and DC, IEEE Trans. Dielectrics Electr. Insul. 22 (2015) 218–228, https://doi.org/10.1109/TDEI.2014.004711.

[33] R. Sarathi, A.J. Reid, M.D. Judd, Partial discharge study in transformer oil due to particle movement under DC voltage using the UHF technique, Electric Power Syst. Res. 78 (2008) 1819–1825, https://doi.org/10.1016/j.epsr.2008.03.022.

[34] A. Noosuk, T. Mermork, A. Semjan, M.S. Rahman, A.R. Dawood, S.B. Ismail, R. D. Kurth, S.R. Atmuri, Commissioning experience of the 300 MW Thailand-Malaysia Interconnection project, in: IEEE/PES Transm. Dist. Conf. Exhib. vol.2 (2002) 1004–1009, https://doi.org/10.1109/TDC.2002.1177614.

[35] S.M. Kayser Azam, A.K.M. Zakir Hossain, M.I. Ibrahimy, S.M.A. Motakabber, Md Shazzadul Islam, M. Othman, Adjacent and diagonal coupling mechanism by even-branched resonator for adjustable radiometric filtering applications, Measurement 202 (2022) 111871, https://doi.org/10.1016/j.measurement.2022.111871.

[36] D. Fahmi, H. Illias, H. Mokhlis, I.M.Yulistya Negara, Particle-triggered Corona Discharge Characteristics in Air Insulation under DC Voltage, 1–1, IEEE Trans. Dielectr. Electr. Insul. (2022), https://doi.org/10.1109/TDEI.2022.3218519.

[37] T. Vu-Cong, C. Toigo, F. Jacquier, A. Girodet, M.N. Tuczek, U. Riechert, A.R. Mor, Long-Term Partial Discharge Behavior of Protrusion Defect in HVDC GIS, IEEE Trans. Dielectr. Electr. Insul. 29 (2022) 2294–2302, https://doi.org/10.1109/TDEI.2022.3206726.

[38] H.A. Illias, M.A. Tunio, A.H.A. Bakar, H. Mokhlis, G. Chen, Partial discharge phenomena within an artificial void in cable insulation geometry: experimental validation and simulation, IEEE Trans. Dielectr. Electr. Insul. 23 (2016) 451–459, https://doi.org/10.1109/TDEI.2015.005155.

[39] C.A. Balanis, Antenna theory: a review, Proc. IEEE 80 (1992) 7–23, https://doi.org/10.1109/5.119564.